Metal Streak Artifacts in X-ray Computed Tomography: A Simulation Study

B. De Man[1], J. Nuyts[2], P. Dupont[2], G. Marchal[3] and P. Suetens[1]
[1]Medical Image Computing, ESAT-PSI, K.U.Leuven, B-3000 Leuven, Belgium
[2]Department of Nuclear Medicine, K.U.Leuven, B-3000 Leuven, Belgium
[3]Department of Radiology, K.U.Leuven, B-3000 Leuven, Belgium

Abstract

Metal streak artifacts are an important problem in X-ray computed tomography. A high-resolution 2D fan-beam computed tomography simulator is presented. Several potential causes of metal streak artifacts are studied using phantom measurements and simulations. Beam hardening, scatter, noise and exponential edge-gradient effect are identified as important causes of metal streak artifacts. Furthermore, also aliasing effects and object motion can be responsible for certain metal streak artifacts.

I. Introduction

In X-ray computed tomography (CT), the presence of strongly attenuating objects - such as dental fillings - causes typical streak artifacts in the reconstructed images (figure 1). Attempts to reduce those streaks are commonly referred to as 'metal artifact reduction (MAR)'. Several researchers have tried to remove metal streak artifacts using various approaches, which - to our knowledge - are all based on the assumption that measured data affected by metal objects are useless for the reconstruction. These 'corrupt' data are either ignored [1, 2] or replaced by synthetic data [1, 3].

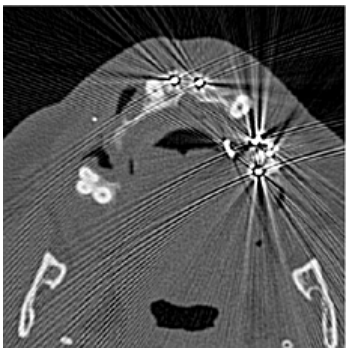

Figure 1: An example of metal streak artifacts in X-ray computed tomography

In our opinion, a complete understanding of the streak generation processes is indispensable for a well-founded solution to the metal streak artifact problem. In CT literature, several causes of (more general) streak artifacts can be found: beam hardening [4, 5, 6, 7, 8, 9], scatter [10, 11], noise [4], exponential edge-gradient effect (EEGE) [12], detector under-sampling [13], view under-sampling [14], object motion [15] and axial partial volume effect [16]. To investigate which of these causes are relevant to metal streak artifacts with modern CT-scanners, we developed a CT simulator and we performed a number of measurements and simulations.

In the following sections we describe the simulator and its validation and we analyze streaks with different origin.

II. Methods

A. Simulator

The simulator is based on a typical fan-beam geometry (figure 2a) and is developed in IDL (Interactive Data Language, Research Systems Inc., Boulder, Colorado). All parameters were adjusted for the Siemens Somatom Plus 4 CT-scanner. The third dimension, perpendicular to the scanning plane, is not taken into account. Spiral artifacts [17, 18, 19] and axial partial volume effects [16] are beyond the scope of this article.

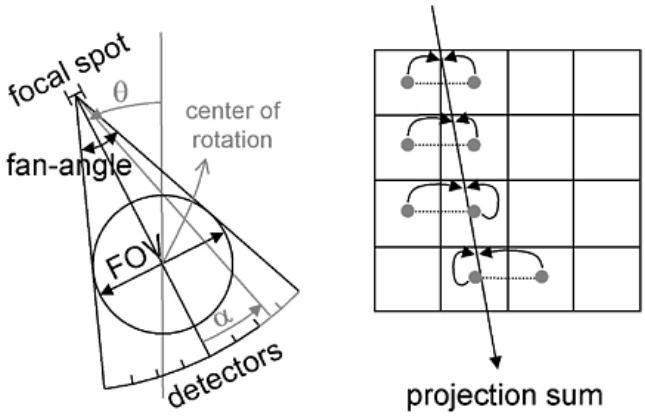

Figure 2: (a) Typical fan-beam CT geometry and (b) projector

The projector (figure 2b) is implemented in C for fast computation: for every detector element the intersections with all rows (or columns) are calculated and the interpolated values are added.

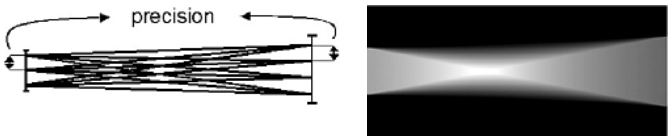

Figure 3: Simulated beam aperture: (a) sampling scheme and (b) resulting intensity distribution

For ease of computation, the X-ray source is modeled as a uniformly radiating straight line. The finite sizes of the focal spot and the detector elements are modeled by sampling at high resolution (typically 0.1mm) followed by a summation of the photon flux over focal spot width (0.6mm) and detector element width (1.2mm). The resulting beam aperture is shown in figure 3.

The spectrum of the X-ray tube is modeled by summing 5 monochromatic simulations at well-chosen energies (figure 4).

Absorption coefficients of water, iron and amalgam are calculated from data available on-line at *http://physics.nist.gov* by averaging over the appropriate parts of the spectrum.

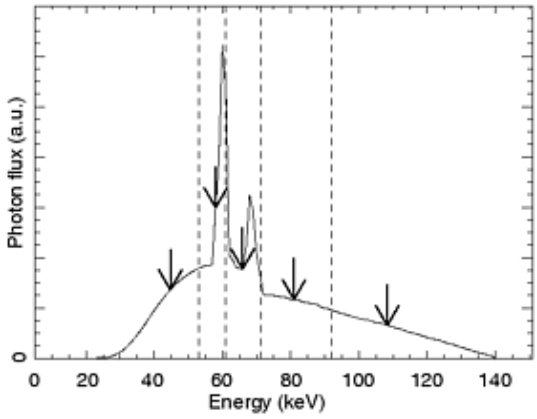

Figure 4: Real (solid line) and simulated (arrows) X-ray spectrum

The continuous rotation of the tube-detector unit is simulated by sampling at small angular (or temporal) intervals followed by a summation of the photon flux over the view angle (or time) interval. Simulations show that the finite integration time is highly determining for the *'line spread function'* (LSF). Measurements of the LSF indicate that this integration time is about $500\mu s$ larger than the expected $710\mu s$. We attribute this excess integration time to the ion collection time, this is the time needed for the ions to drift towards the measuring electrodes in the Xenon detectors. This result is in good agreement with the theoretical ion collection time of $600\mu s$ calculated as $t_{coll} = \frac{(\Delta x)^2}{k\ V}$ where Δx is the inter-electrode distance, V the applied voltage and $k = 0.015\frac{cm^2}{V \cdot s}$ the ionic mobility taken from [20]. This so-called *'after-glow* effect' is modeled by adding to each view an appropriate number of samples from the next view.

According to the manufacturers, all non-linearities in the detector response are perfectly compensated for. Detector cross-talk is modeled by including a detector overlap of 1/6 at both sides. The detector array is shifted over one fourth of the detector element width to remove the redundancy inherent to a standard 360^o fan-beam acquisition.

In accordance with [10, 11] a constant scatter level was chosen. Real scatter profiles usually contain very little high frequencies, and therefore, a constant scatter profile is expected to be a good approximation, at least for the purpose of this article.

Poisson noise was added to the simulated intensities. The noise level was tuned so that the simulated intensities had the same standard deviation as in the measurements.

B. Validation

1) LSF

We determined the LSF of both the real CT scanner and the simulator, using an iron wire (ø 0.7mm) positioned at different positions perpendicular to the scanning plane. The full width at half maximum (FWHM) of the LSF was calculated by fitting a Gaussian.

2) phantoms

A number of phantoms were measured and simulated. A first phantom consisted of a water bowl and a cylindrical iron rod (ø 11.6mm) positioned eccentrically in the water. The second series of phantoms consisted of a Plexiglas plate, with one, two or three cylindrical amalgam fillings. Figure 5 shows two reconstructions from artifact-free simulations (a) for the water bowl with iron rod (*phantom 1*) and (b) for the plexi plate with three amalgam fillings (*phantom 2*).

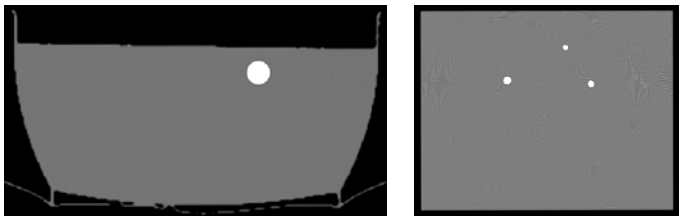

Figure 5: Artifact-free simulations: (a) *phantom 1*: water bowl with iron rod and (b) *phantom 2*: plexi plate with 3 amalgam fillings

C. Reconstruction

Two reconstruction algorithms have been implemented. The first is the direct fan-beam filtered backprojection algorithm from Herman [21]. The backprojector (figure 6) is implemented in C for fast computation: for every pixel, the intersection with the detector array is computed. The corresponding interpolated value is assigned to the pixel.

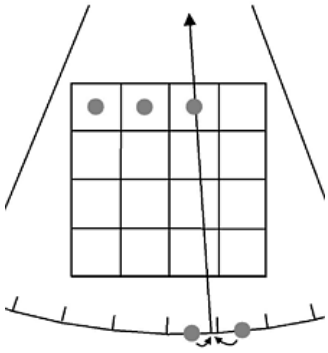

Figure 6: Backprojector

A second reconstruction algorithm consists of a rebinner followed by a parallel beam reconstruction. This was used only for validation of the direct fan-beam reconstruction.

D. Streak Analysis

The effect of beam hardening was investigated by comparing polychromatic and monochromatic simulations. For the latter, attenuation coefficients of the phantoms were defined so that the resulting intensities were in the same order of magnitude as in the polychromatic case.

Similarly, the effects of scatter, noise and exponential

edge-gradient effect (EEGE) were investigated by comparing scatter-, noise- and EEGE-free simulations and simulations *with* scatter, noise or EEGE. The scatter-to-primary ratio was arbitrarily chosen to be 0.0001. The noise level was determined by choosing an unattenuated flux of 10^5 or 2×10^5 photons per detector, depending on the phantom. Under these circumstances, both the standard deviations in the projections and the degree of artifact were comparable to those in the measured data.

The effect of noise was also investigated by scanning a phantom multiple times under identical circumstances. Averaging of n intensity sinograms allows to reduce the noise by a factor $\sqrt{n}$. Averaged images and original images were compared.

The EEGE needs some further explanation (see also [12]). Two modes of simulation were used. In the first mode, the projection sums are calculated as the logarithm of the integral over the focal spot and over the detector elements of the photon flux:

$$p = -\ln \frac{\int_A \int_B I_0 \cdot exp(-\int_{L_{a,b}} \mu(s)\, ds)\, da\, db}{A \cdot B \cdot I_0} \qquad (1)$$

where I_0 is the un-attenuated intensity, A and B the areas of focal spot and detector, μ the attenuation coefficient and $L_{a,b}$ the line defined by a and b. This is the correct simulation procedure. In the second mode, the projection sums are calculated as the mean over the focal spot and over the detector elements of the attenuation line integrals.

$$p = \frac{1}{A}\frac{1}{B} \int_A \int_B (\int_{L_{a,b}} \mu(s)\, ds)\, da\, db \qquad (2)$$

This second mode allows to eliminate the EEGE.

The influence of motion of the scanned object was simulated by calculating two sinograms for the object at two slightly different positions and taking a part of both sinograms to synthesize a new sinogram.

Influence of detector and view sampling was investigated by reconstructing an image making use of data from only a subset of the detectors or of the views.

III. Results & Discussion

A. Validation

A good Gaussian fit of the LSF was obtained in most projections (except where the projection of the wire coincides with the border of the patient table).

Good agreement was obtained between measured and simulated FWHM of LSF as a function of view angle (figure 7). The typical cyclic behaviour has an easy intuitive explanation: The width of the LSF depends mainly on three parameters: the distance $\overline{IF}$ from the iron wire to the focal spot, the distance $\overline{IC}$ from the iron wire to the center of rotation and the angle γ between (1) the beam through the iron wire and (2) the line connecting the iron wire and the center of rotation. Distance

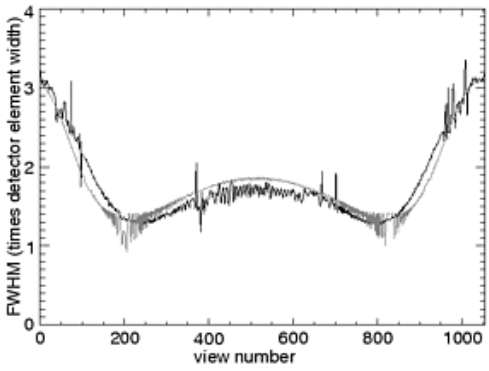

Figure 7: FWHM of the LSF versus view number: measured (black) and simulated (gray)

$\overline{IF}$ determines the beam width and the distance between two consecutive beams at that particular position. Distance $\overline{IC}$ and angle γ determine the speed at which a beam sweeps by at that particular position: $v_{sweep} = v_{angular} \cdot \overline{IC} \cdot cos(\gamma)$.

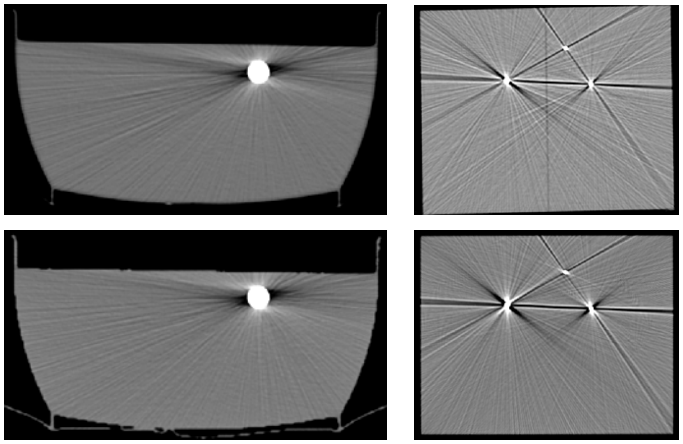

Figure 8: Water bowl with iron rod (left) and plexi plate with 3 amalgam fillings (right): measured (top) versus simulated (bottom)

Good agreement is obtained between measured and simulated images for both *phantom 1* and *phantom 2* (figure 8). All reconstructions are windowed in the interval $\mu = [0.1; 0.3]\ cm^{-1}$.

B. Beam Hardening

Figure 9 shows the polychromatic simulations. For *phantom 1*, we observe dark streaks in the directions of highest attenuation. Also the more general cupping artifact is present, but this can not be seen with the current windowing. In the case of two or more metal objects (*phantom 2*) additional dark streaks connecting the metal objects can be seen.

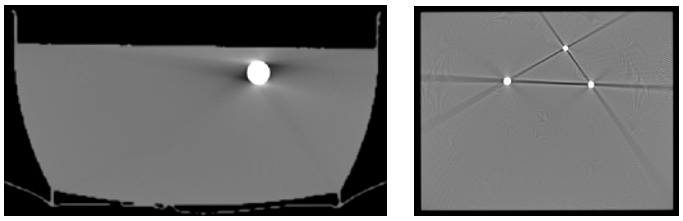

Figure 9: Polychromatic simulations: (a) *phantom 1* and (b) *phantom 2*

C. Scatter

Figure 10 shows the simulations with added constant-level scatter. For *phantom 1*, we observe dark streaks in the directions of highest attenuation. Again, also cupping is present but not visible with the current windowing. For *phantom 2*, additional streaks connecting the metal objects can be seen. Even a very small scatter-to-primary ratio causes significant streaks. Also some bright streaks are present bordering the dark streaks. This is probably due to the negative values in the reconstruction kernel. Note that these artifacts are very similar as the polychromatic artifacts in figure 9 (see also [10] and [11]).

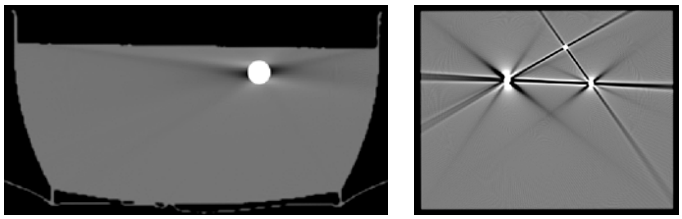

Figure 10: Simulation with constant-level scatter: (a) *phantom 1* and (b) *phantom 2*

D. Exponential Edge-gradient Effect

Figure 11 shows simulations with the exponential edge-gradient effect. For *phantom 1*, no streaks are observed. For *phantom 2*, dark streaks can be seen connecting edges with equally-signed gradients, while white streaks can be seen connecting edges with opposite gradients. More generally, the EEGE is known to cause streaks tangent to long straight edges. For instance, using different windowing, dark streaks can be seen along the edges of the plexi plate. Additionally, a number of streaks can be seen radiating from the metals.

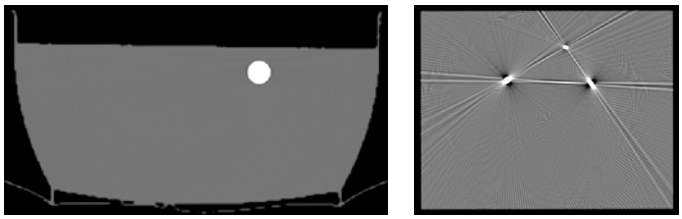

Figure 11: Simulation with EEGE: (a) *phantom 1* and (b) *phantom 2*

E. Noise

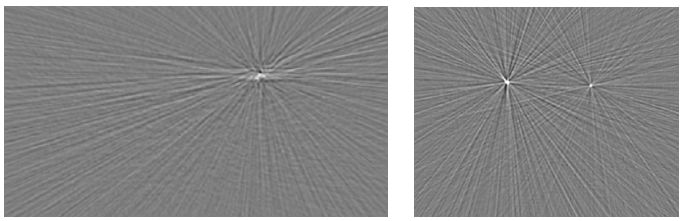

Figure 12: Error due to noise determined by simulations with and without noise: (a) *phantom 1* and (b) *phantom 2* (windowing: $\mu = [-0.05; 0.05]\ cm^{-1}$)

Figure 12 shows the error due to noise determined from simulations with and without noise. Streaks can be seen in directions of highest attenuation and connecting metal objects. This type of streaks consists of thin lines alternately dark and bright and are also distinguishable in figure 8. Noise artifacts are non-linear artifacts, just like beam hardening and scatter artifacts ([4]). The degree of artifact strongly depends on the magnitude of the measured intensities and thus of the total integrated attenuation. As a consequence, even the amount of scatter and beam hardening have a strong influence on the severity of the noise artifacts.

F. Motion

Figure 13 shows a simulation where the iron rod was moved over about 1.4mm after 700 views. Streaks can be seen in two directions: from the rod to the focal spot at the two positions of inconsistency, this is between view 700 and view 701 and between view 1056 and view 1.

Figure 13: Simulation of object motion

G. Aliasing

Figure 14a shows a simulation of *phantom 1* using only half of the detectors for the reconstruction. Clearly, typical artifacts due to detector under-sampling (circular patterns tangent to strong edges) can be seen. Similarly, figure 14b shows a simulation of *phantom 1* using only a quarter of the views for the reconstruction. Again typical artifacts due to view under-sampling (streaks starting at a certain distance from the center) are observed.

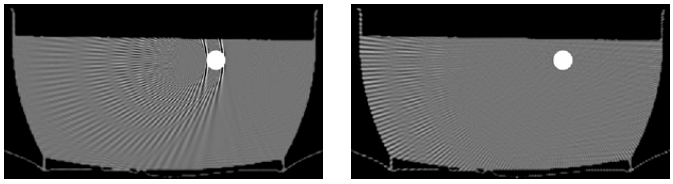

Figure 14: Simulations with (a) detector under-sampling and (b) view under-sampling

Note that even in the 'artifact-free' simulations (figure 5), aliasing errors (such as Moire patterns) are present, although not visible with the current windowing. However, appropriate reconstruction kernels should be able to reduce aliasing artifacts as much as wanted, possibly at the expense of the spatial resolution of the reconstruction.

Moreover, neither the aliasing artifacts, nor the artifacts due to object motion are limited to the case of metal objects, but because of their high attenuation values, the presence of metal objects makes the artifacts more prominent.

IV. Future Work

For the scope of this article, we focussed on one specific scanner type. Results must be generalized for other scanner

types. Extension to 3D, and in particular analysis of the axial partial volume effect is needed.

The next step is to try to reduce streak artifacts. One possible approach is to prevent artifacts during the acquisition. Noise can be reduced by using high mAs-settings. Beam hardening can be minimized by using pre-filtering. The partial volume effect due to z-gradients can be reduced by making thin slices. Unfortunately, all these measures are in direct conflict with other clinical concerns such as low patient dose, tube life, etc ...

Our aim is to apply iterative reconstruction [19] to reduce metal streak artifacts. The major advantage of this approach is the possibility to use a model of the acquisition, taking into account polychromaticity, scatter, noise, EEGE and any other imperfections. A general iterative reconstruction scheme is shown in figure 15.

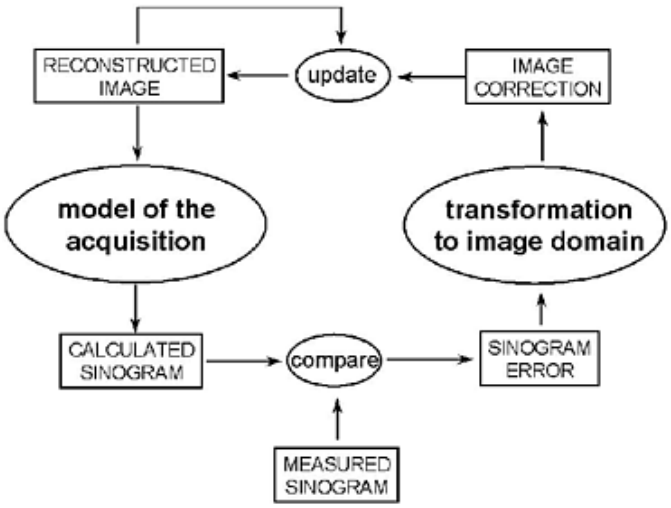

Figure 15: Iterative Reconstruction

V. Conclusions

A high-resolution 2D CT simulator has been developed and validated. We have proven that all investigated causes of streaks are effectively able to produce streaks. Beam hardening, scatter, noise and EEGE are the most important causes of metal streak artifacts. Under extreme circumstances, also object motion and aliasing effects produce streak artifacts. Artifacts due to axial gradients need further investigation.

VI. Acknowledgments

This work is supported by the Flemish Fund for Scientific Research (FWO), grant number G.0106.98. P. Dupont is post-doctoral researcher of the FWO. We wish to thank the people from Siemens (Forchheim) for the information about their CT scanners. We also wish to thank François De Cock, Patrick Lievens and Philippe Vervloesem (Dept. of Radiology) for their professional assistance in the experiments. Finally, we wish to thank Els Tijskens for the production of the Plexiglas phantom and Anne Vander Speeten for the use of the water phantom.

VII. References

[1] D.D.Robertson, J.Yuan, G.Wang and M.W.Vannier, "Total Hip Prosthesis Metal-Artifact Suppression Using Iterative Deblurring Reconstruction," *J. Comput. Assist. Tomogr., vol. 21, 1997* pp. 293-298

[2] G.Wang, D.L.Snyder, J.A.O'Sullivan and M.W.Vannier, "Iterative Deblurring for CT Metal Artifact Reduction," *IEEE Trans. Med. Imaging, vol. 15, 1996* pp. 657-664

[3] W.A.Kalender, R.Hebel and J.Ebersberger, "Reduction of CT Artifacts Caused by Metallic Implants," *Radiol., vol. 164, 1987* pp. 576-577

[4] A.J.Duerinckx and A.Macovski, "Nonlinear Polychromatic and Noise Artifacts in X-Ray Computed Tomography Images," *J. Comput. Assist. Tomogr., vol. 3, 1979* pp. 519-526

[5] A.J.Duerinckx and A.Macovski, "Polychromatic Streak Artifacts in Computed Tomography Images," *J. Comput. Assist. Tomogr., vol. 2, 1978* pp. 481-487

[6] P.M.Joseph and R.D.Spital, "A Method for Correcting Bone Induced Artifacts in Computed Tomography Scanners," *J. Comput. Assist. Tomogr., vol. 2, 1978* pp. 100-108

[7] D.D.Robertson and H.K.Huang, "Quantitative bone measurements using x-ray computed tomography with second-order correction," *Med. Phys., vol. 13 no. 4, 1986* pp. 474-479

[8] J.M.Meagher, C.D.Mote and H.B.Skinner, "CT Image Correction for Beam Hardening Using Simulated Projection Data," *IEEE Trans. Nucl. Sci., vol. 37 no. 4, 1990* pp. 1520-1524

[9] P.M.Joseph and C.Ruth, "A method for simultaneous correction of spectrum hardening artifacts in CT images containing both bone and iodine," *Med. Phys., vol. 24 no. 10, 1997* pp. 1629-1634

[10] P.M.Joseph and R.D.Spital, "The effects of scatter in x-ray computed tomography," *Med. Phys., vol. 9, 1982* pp. 464-472

[11] G.H.Glover, "Compton scatter effects in CT reconstructions," *Med. Phys., vol. 9, 1982* pp. 860-867

[12] P.M.Joseph and R.D.Spital, "The exponential edge-gradient effect in x-ray computed tomography," *Phys. Med. Biol., vol. 26, 1981* pp. 473-487

[13] P.M.Joseph, R.D.Spital and C.D.Stockham, "The effects of sampling on CT images," *Computerized Tomography, vol. 4, 1980* pp. 189-206

[14] P.M.Joseph and R.A.Schulz, "View sampling requirements in fan beam computed tomography," *Med. Phys., vol. 7, 1980* pp. 692-702

[15] G.H.Glover and N.J.Pelc, "An algorithm for the reduction of metal clip artifacts in CT reconstructions," *Med. Phys., vol. 8, 1981* pp. 799-807

[16] G.H.Glover and N.J.Pelc, "Nonlinear partial volume artifacts in x-ray computed tomography," *Med. Phys., vol. 7 no. 3, 1980* pp. 238-248

[17] G.Wang and M.W.Vannier, "Stair-Step Artifacts in Three-dimensional Helical CT: An Experimental Study," *Radiol., vol. 191 no. 1, 1994* pp. 79-83

[18] J.A.Brink, ”Technical aspects of helical (spiral) CT,” *Radiologic Clinics of North America, vol. 30 no. 5, 1995* pp. 825-841

[19] J.Nuyts, B.De Man, P.Dupont, M.Defrise, P.Suetens and L.Mortelmans, ”Iterative reconstruction for helical CT: a simulation study,” *Phys. Med. Biol., vol. 43, 1998* pp. 729-737

[20] D.J.Drost and A.Fenster, ”A xenon ionization detector for digital radiography,” *Med. Phys., vol. 9 no. 2, 1982* pp. 224-230

[21] G.T.Herman, ”Image Reconstruction From Projections,” *Orlando: Academic Press, 1980, pp. 161-179*